Vol. (2), No (1), January-March 2025 DOI:10.21608/MERMJ.2025.380096.1025

Design, Synthesis, Anti-cancer Screening, Mechanistic, and Molecular Modeling Studies of *N*-(3-methoxyphenyl)-2-(4-oxo-1-phenyl-1,4-dihydro-*5H*-pyrazolo[3,4-*d*]pyrimidin-5-yl) Acetamide.

Mostafa R. Kobesy[1 *], Mamdouh F. A. Mohamed[2], Eman A.M. Beshr[3], Aliaa M. Mohassab[3].

[1] Department of Medicinal Chemistry, Faculty of Pharmacy, Merit University, Sohag, Egypt.
[2] Department of Medicinal Chemistry, Faculty of Pharmacy, Minia University, Minia 61519, Egypt.
[3] Department of Pharmaceutical Chemistry, Faculty of Pharmacy, Sohag University, Sohag 82524, Egypt
[*]Corresponding author. Mostafa R. Kobesy.

ARTICLE INFO

Article History:
Received: 29 April 2025
Accepted: 1 June 2025
Available online: 18 June 2025

Keywords:

Pyrazolo[3,4-d]pyrimidinone, anti-cancer, CDK1, CDK2, apoptosis, Molecular modeling study.

Abstract

A newly developed pyrazolo[3,4-d]pyrimidinone derivative was produced, characterized, and evaluated for its ability to combat cancer. The compound demonstrated significant anti-cancer effects, completely halting the growth of renal RXF-393 cancer cells and inhibiting 91.04% of growth in non-small cell lung (NSCL) HOP-92 cancer cells. Notably, the compound exhibited less toxicity towards normal cells (WI 38) compared to staurosporine, with IC50 values of 44.893±2.55 µM and 13.610±0.77 µM, respectively, indicating its selective action against cancer cells. Mechanistic studies revealed the compound's potent inhibitory activity against CDK1 and CDK2, with IC_{50} values of 0.385±0.021 µM and 0.58±0.018 µM, respectively, compared to roscovitine (IC_{50} values of 0.803±0.044 µM and 1.072±0.033 µM). Molecular modeling studies corroborated the compound's strong interactions and indicated favorable drug-like properties. The results of this study suggest that the compound holds promise and could be valuable in creating new therapies to combat cancer.

1. Introduction

Cancer, a genetic disorder characterized by uncontrolled cell proliferation and the potential to invade other tissues (metastasis), arises from dysregulation of cellular growth, leading to tumor formation.[1]. The projected threefold increase in cancer incidence by 2050 underscores the critical need for new anti-cancer drugs to combat its global spread [2]. Pyrazolo[3,4-d]pyrimidine, a purine isostere, has garnered significant concern in drug development due to its versatile nature as a pharmacophore [3]. The use of the pyrazolo[3,4-d]pyrimidine scaffold in drug design has been shown to enhance various biological activities, including

anti-inflammatory [4], antimicrobial [5], anti-mycobacterial [6], antimalarial, antiviral [7], anti-gout [8], and anti-diabetic effects [9]. Notably, pyrazolo-pyrimidine rings may exhibit activity against various cancer cells. Their primary application lies in their anti-cancer properties, achieved through the inhibition of key targets and enzymes involved in cancer development [10], particularly cyclin-dependent kinases (CDKs) such as CDK1 [11], CDK2 [12], and EGFR [13], as well as Src kinase [14] and m-TOR [15]. While known as a serine/threonine protein kinase, CDK1's functions extend beyond just controlling the cell cycle; it is also involved in critical processes such as regulating gene expression and apoptosis [16, 17]. In addition to its involvement in cell cycle progression, CDK2 aids in assembling cyclin-dependent protein kinase complexes [18]. As a result, inhibiting CDK2 is viewed as a hopeful approach for the creation of new medications to fight cancer [19, 20]. Several drugs have been developed to inhibit these kinases; for instance, palbociclib, used to treat advanced breast cancer, targets CDK1 and CDK2, highlighting the therapeutic potential of CDK inhibition in oncology [21, 22]. Roscovitine is another potent CDK2 inhibitor that has demonstrated efficacy in inducing neoplastic cell death [23]. Previous research has shown that various derivatives possess potent anticancer activity, with some compounds showing activity through CDK1 inhibition [11], such as compound I, that represented in Figure **1**, and others through CDK2 inhibition, as compound II [24] **Figure 1**. a novel N-5-substituted-pyrazolo[3,4-d]pyrimidinone compound was synthesized as a prospective agent against cancer. The National Cancer Institute (NCI) in Bethesda, USA, assessed the antitumor effects of this compound across 60 different cancer cell lines, adhering to established NCI protocols. The compound was selected for IC50 determination against cell lines exhibiting significant growth inhibition. Furthermore, cell cycle analysis and apoptosis studies were conducted to investigate the mechanisms underlying its anti-cancer effects. Additionally, the compound's activity against CDK1 and CDK2 enzymes was assessed to explore its potential mechanism of action in comparison to roscovitine.

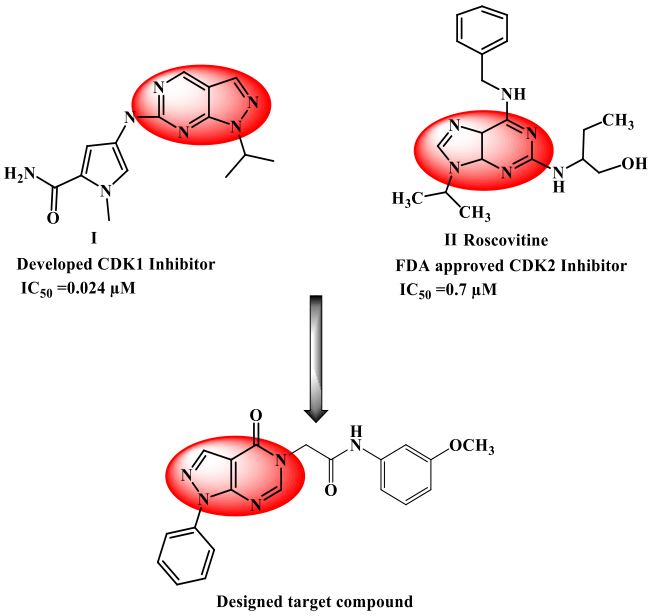

Figure 1. Structures of representative compound **I** as a CDK-1 inhibitor, compound **II** as a CDK-2 inhibitor, and the designed target compound.

2. Experimental section

2.1. Chemistry

Scheme 1 illustrates the series of chemical transformations employed in the synthesis of an N-alkylated pyrazolo[3,4-d]pyrimidin-4(5H)-one derivative. The synthesis of **Compound 1** was carried out based on a literature procedure [25]. This involved the reaction of triethyl orthoformate and malononitrile using acetic anhydride under reflux conditions. Subsequently, the obtained mixture underwent a reflux reaction with phenyl hydrazine in ethanol, which resulted in the creation of 5-amino-1-aryl-1H-pyrazole-4-carbonitriles 2 [26]. The desired key intermediate **3** [26] was obtained by subjecting compound **2** to cyclization in refluxing formic acid. To obtain the 2-chloro-N-phenylacetamide derivatives **4**, the appropriate amine derivative was reacted with chloroacetyl chloride. This reaction was

DOI:10.21608/MERMJ.2025.380096.1025

carried out in acetic acid with sodium acetate serving as the base, resulting in the required intermediates **4** [27]. The structures of the synthesized intermediates 1 through 4 were confirmed by comparing their melting points with previously reported values [25-28]. Compound **3** was reacted with compound 4 in refluxing DMF in the presence of anhydrous K_2CO_3, resulting in alkylation at the NH position, giving the desired final compound, N-(3-methoxyphenyl)-2-(4-oxo-1-phenyl-1,4-dihydro-5H-pyrazolo[3,4-d]pyrimidin-5-yl)acetamide [29]. The purity of these new compounds was validated using IR, ^{1}HNMR, ^{13}CNMR, and elemental methods of analysis. The ^{1}HNMR analysis of the target compound revealed several significant singlet signals at δ 10.48 ppm (N-H), δ 8.52 ppm (pyrimidine-H), δ 8.41 ppm (pyrazole-H), and δ 4.93 ppm (CO-CH2). The aromatic protons (9H) resonated between δ 8.08 and 7.11 ppm. The target compound's ^{13}C NMR spectrum showed two distinctive peaks at δ 160.28 ppm and δ 156.84 ppm, corresponding to the carbonyl groups (CH2-C=O-N- of the amide and C=O of the pyrimidin-4-one ring, respectively). A distinct peak at δ 48.72 ppm corresponded to the carbon of the methylene group linked to N-3 of the pyrimidinone ring (N-CH_2-CO). Furthermore, the IR spectra of the target molecule revealed a large stretching band at 3420 cm^{-1}, which corresponded to (NH). Two stretching bands emerged at 1585 and 1684 cm^{-1} as a result of the presence of two carbonyl groups (C=O of the amide and C=O of the pyrimidinone ring).

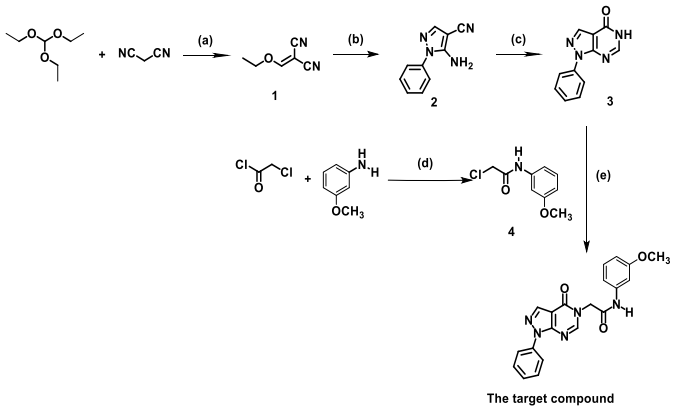

Scheme (1). Synthesis of *N*-(3-methoxyphenyl)-2-(4-oxo-1-phenyl-1,4-dihydro-5*H*-pyrazolo[3,4-*d*]pyrimidin-5-yl)acetamide.

The following reagents and reaction conditions were employed: (a) Acetic anhydride, reflux 4 h; **(b)** C_6H_5-$NHNH_2$, EtOH, reflux 18 h; **(c)** formic acid, reflux 4-5 h; **(d)** appropriate aromatic amine, glacial acetic acid, chloroacetyl chloride, 0 ^{o}C (for 0.5 h) then RT (for 1 h), CH_3COONa; **(e)** K_2CO_3, DMF, reflux, 8 h.

2.2. Biology

2.2.1. A single-dose anticancer screen of the target compound 1 was carried out by the NCI.

Motivated by the promising anticancer properties of the Pyrazolo-Pyrimidinone derivative, we decided to evaluate its potential antitumor effects following the standard anticancer screening protocols of the NCI's Drug Evaluation Section [31]. At a 10 µM concentration, the target compound was assessed for its capacity to curb the growth of sixty cancer cell lines. The screening results indicated considerable anticancer activity against specific cell lines, illustrated in **Figure 2**.

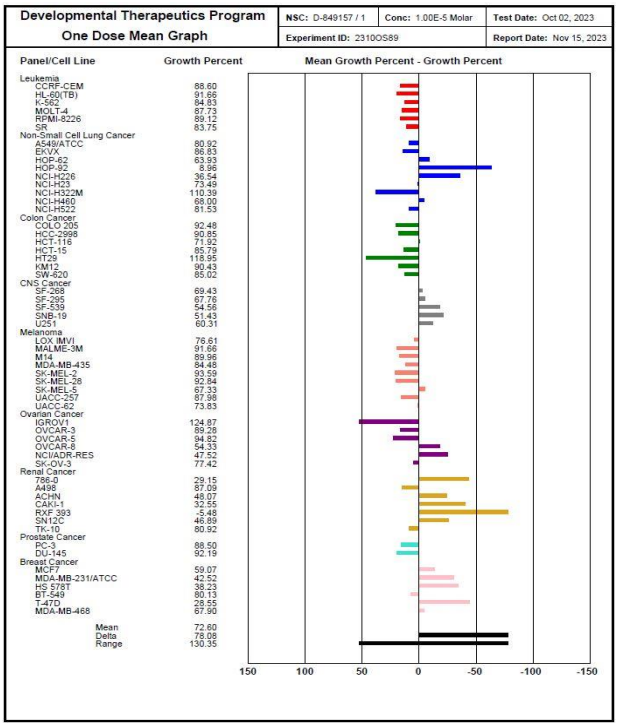

Figure 2. A single-dose anticancer screen of compound **1** was conducted at 10 µM by the NCI in Bethesda, USA

The data presented in **Figures 2 and 3** indicate that the target drug has a substantial anticancer effect on the RXF-393 renal cancer cell line, leading to complete growth inhibition and some cancer cell death. The target chemical also has strong effectiveness against non-small cell lung cancer (HOP-92), suppressing growth by 91.04%. Furthermore, good action was seen against NCI-H226, ovarian NCI/ADR-RES, renal 760-0, ACHN, CAKI-1, SN12C, breast cancer cell lines, with growth inhibition of more than 50%. The substantial anticancer activity of the desired compound, notably against the kidney cancer cell line, encourages us to perform a more detailed mechanistic study. This will encompass cell cycle analysis, apoptosis assessment, and an evaluation of its CDK1/2 inhibition.

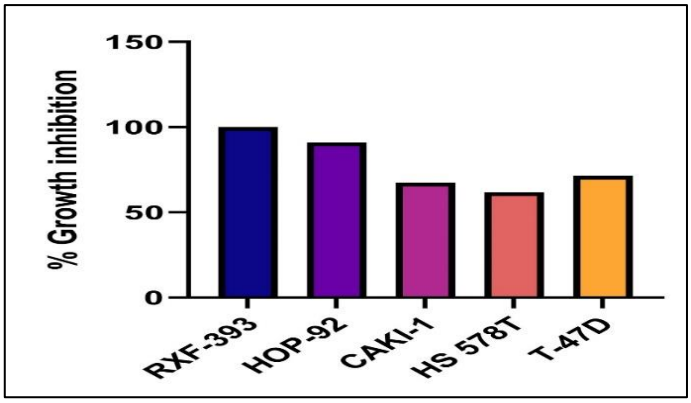

Figure 3. The important anticancer screening data for the target compound, evaluated at a single 10 µM concentration against the RXF-393, HOP-92, CAKI-1, HS 578T, and T-47D cancer cell lines, are highlighted.

2.2.2. The effect of the desired compound on cell survival was evaluated in the cancerous renal RXF-393 and NSCL HOP-92 cell lines, and also in the non-cancerous WI 38 cell line.

In vitro screening revealed that the target compound potently inhibited the growth of renal RXF393 cells (IC50 = 17.88±1.32 µM) and displayed less pronounced activity against lung HOP-92 cells (IC50 = 29.37±1.87 µM). Staurosporine, used as a reference, demonstrated superior growth inhibition in both cell lines (RXF-393: IC_{50} = 3.27±0.19 µM; HOP-92: IC_{50} = 4.54±0.26 µM). This compound showed a greater safety margin than doxorubicin when tested on normal WI 38 cells, with IC_{50} values of 44.893±2.55 µM and 13.893±0.77 µM, respectively. These findings suggest that the target compound demonstrates higher selectivity towards cancer cell lines with lower harm to normal human cells compared to staurosporine, indicating its potential for developing novel anticancer agents (**Table 1)** [32].

Table 1: The IC50 values (µM ±SEM), indicating in vitro cytotoxicity, were determined for the target compound using human renal (RXF-393) and NSCL (HOP-92) cancer cell lines, alongside the normal WI 38 cell line. The results were compared to the cytotoxicity profile of the standard anticancer agent staurosporine.

Compound	**Cytotoxicity IC_{50} (µM)**		
	HOP-92	RXF-393	WI-38 normal cell line
The target compound	29.37±1.8	17.88±1.32	44.89±2.55
Staurosporine	4.54±0.26	3.27±0.19	13.61±0.77

2.2.3. CDK inhibitory activity assay

The significant CDK-inhibiting potential of this scaffold framework accounts for its widespread use as a scaffold in drug research [33]. The target compounds' in vitro inhibitory effects on CDK1 and CDK2 enzymes were measured and compared to those of the known CDK inhibitor, roscovitine [23]. The inhibitory activity of the target compound against CDK1 and CDK2 enzymes was evaluated, with roscovitine used as a reference for comparison, as in (**Table 2)** [23]. The target compound demonstrated greater inhibitory activity against CDK1 and CDK2 compared to the reference drug roscovitine. Roscovitine exhibited half-maximal inhibitory concentrations (IC50) of 0.803µM and 1.072 µM for CDK1 and CDK2, respectively. In contrast, the target compound displayed lower IC50 values of 0.385µM against CDK1 and 0.58 µM against CDK2, indicating enhanced potency. The findings from this assay indicate a potential link between the target compound's anti-proliferative properties and its inhibitory activity against CDK1 and CDK2. It is plausible that the compound exerts its effect by blocking the activity of these two crucial cell cycle regulators.

Compound	**CDK1 IC_{50}(µM)**	**CDK2 IC_{50}(µM)**
The target compound	0.385±0.021	0.58±0.018
Roscovitine	0.803±0.044	1.072±0.033

Table 2: The IC50 values (µM) of the target compound and roscovitine against CDK1 and CDK2 are compared.

2.2.4. Cell cycle analysis

Regulation of the cell cycle is a primary determinant of cell proliferation. y causing tumor cells to stop progressing through the cell cycle, their proliferation can potentially be reduced. Flow cytometry was utilized to analyze the cell cycle progression of RXF393 and HOP-92 cancer cell lines after treatment with an IC50 concentration of the target compound. Untreated RXF393 and HOP-92 cells served as negative controls in this assessment [34] (**Table 3 and Figure 4**).

Sample	**DNA content**			
	%G0-G1	**%S**	**%G2/M**	**Comment**
Target compound/HOP-92	52.71	22.35	**24.94**	Cell growth arrest at G2/M
DMSO.HOP-92	61.07	25.64	13.29	-
Target compound/RXF-393	**56.39**	37.11	6.5	Cell growth arrest at G1
DMSO.CRXF-393	46.32	42.88	10.8	-

Table 3: The proportion of cells in each phase of the cell cycle, as determined by DNA content, was evaluated in NSCLC (HOP-92) and renal (RXF-393) cancer cell lines treated with either the control (DMSO) or the target compound

DOI:10.21608/MERMJ.2025.380096.1025

The study demonstrated a notable G2/M cell cycle arrest in HOP-92 cells, with the percentage increasing from 13.29% to 24.94%. This finding indicates that the treatment resulted in cell cycle arrest at the G2/M checkpoint in these cells. In RXF-393 cells, treatment with the target compound at its IC50 concentration caused a significant increase in the G0-G1 phase cell population, from an initial 46.32% to 56.39%. This observation implies that the compound induces G1 phase cell cycle arrest in this cell line see (**Table 3** and **Figure 5)**.

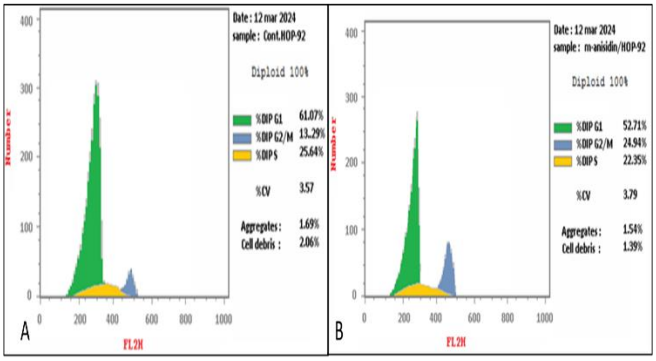

Figure 4. Cell cycle phase distribution of NSCLC (HOP-92) cells treated with DMSO (Control, A) versus the target compound (IC50, 29.37 µM). Compound (IC50, 29.37 µM).

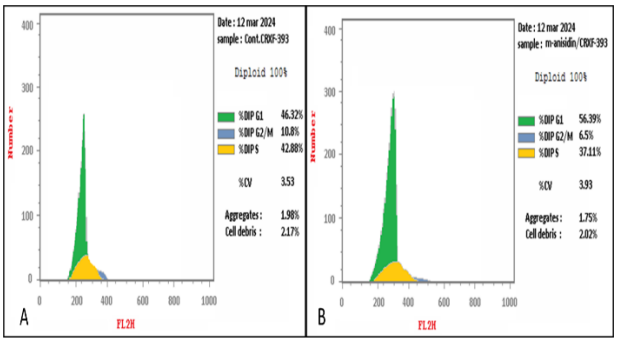

Figure 5. The impact of treating renal (RXF 393) cells with a DMSO control (A) versus the target compound (at an IC50 of 17.88 µM) on the accumulation of cells in different cell cycle stages.

2.2.5. Apoptosis assay

The controlled process of cell death, known as programmed cell death or apoptosis (and sometimes referred to as "cellular suicide"), allows healthy organisms to get rid of unneeded cells. A hallmark of cancer is the evasion of apoptosis, contributing to the survival of malignant cells [35]. Apoptosis, a multifaceted process with diverse pathways, is critical in preserving cellular homeostasis. Aberrations in apoptotic pathways can not only drive malignant transformation but also compromise the efficacy of cancer therapies [35]. To determine if the observed anti-proliferative effects of the target compound on Hop-92 and RXF-393 cell lines were linked to the induction of cell death, we investigated its potential to trigger apoptosis and necrosis in these cells. Following a 24-hour incubation with the target compound at its respective IC_{50} concentrations, flow cytometric analysis revealed a substantial induction of necrosis, early apoptosis, and late apoptosis in both the HOP-92 (5.45%, 9.55%, and 3.92%, respectively) and RXF-393 (3.99%, 15.29%, and 7.03%, respectively) cell lines (**Table 5**, **Figures 6** and **7)**.

	Conc IC_{50} (µM)	Apoptosis			Necrosis
		Total	Early	Late	
The target compound/ HOP-92	29.37±1.9	18.92	9.55	3.92	5.45
DMSO.HOP-92	---	1.87	0.27	0.19	1.41
The target compound /RXF-393	17.88±1.3	26.31	15.29	7.03	3.99
DMSO.RXF-393	---	2.19	0.65	0.13	1.41

Table 4: Assessment of the target compound's ability to induce apoptosis in HOP-92 and RXF-393 cancer cell lines.

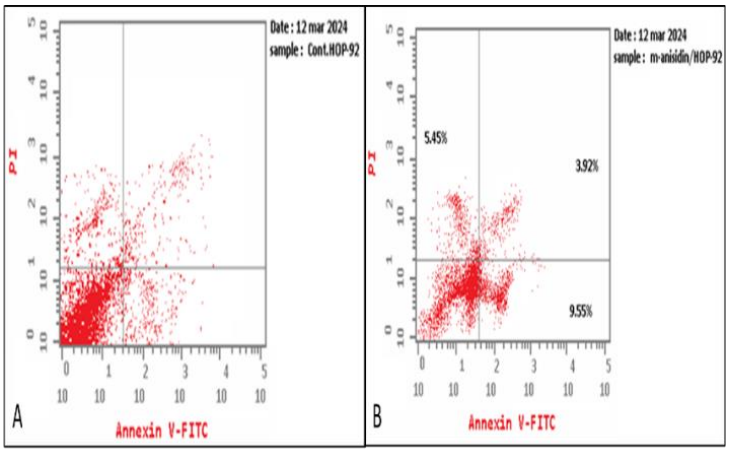

Figure 6. The assessment of apoptosis and necrosis in non-small cell lung cancer HOP-92 cells induced by the control (DMSO, A) and the target compound at its IC50 concentration (29.37 µg/mL, B).

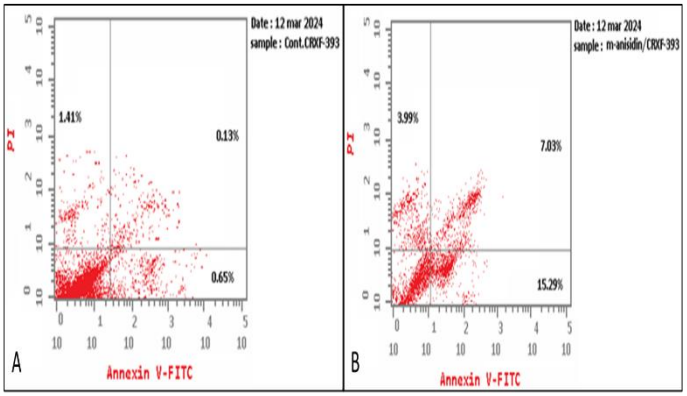

Figure 7. The assessment of apoptosis and necrosis in renal RXF-393 cells induced by the control (DMSO, A) and the target compound at its IC50 concentration (17.88 µM, B).

2.2.6. Molecular modeling

2.2.6.1. Target identification

The potential anticancer target of the synthesized compound was initially investigated using a pharmacophore-based virtual screening strategy on the PharmMapper platform [https://www.lilab-ecust.cn/pharmmapper/ [36]. PharmMapper predicts potential protein targets for a given molecule by assessing the spatial congruence between the molecule's key pharmacophoric features and those of known The probability of interaction with an identical protein increases with the degree of alignment. Consequently, the target compound's structure was analyzed using PharmMapper to identify potential protein targets related to its anticancer activity. The resulting protein targets were ranked according to their "Fit score" **Figure 8**, which indicates the quality of the pharmacophore match. Notably, human cyclin-dependent kinase 1 (CDK-1) [37] and human cyclin-dependent kinase 2 (CDK-2) [38] emerged as high-ranking potential targets, displaying Fit scores of 15.08 and 16.03, respectively **Figure 8.**

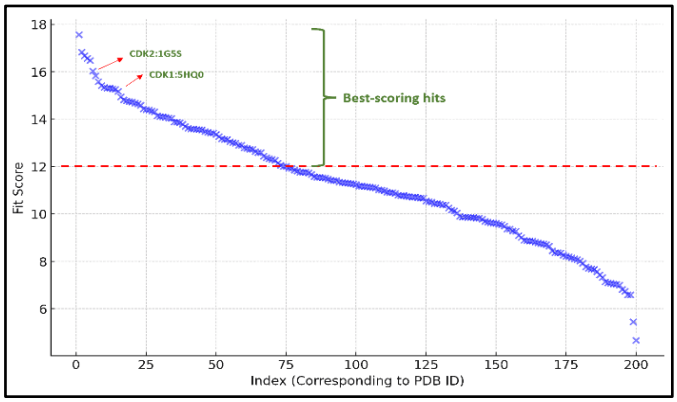

Figure 8. The PharmMapper analysis yielded a scatter plot visualizing potential protein targets for the synthesized compound, ranked by their Fit scores. Employing a selection threshold of 12 for the Fit score, the analysis highlighted human cyclin-dependent kinase 1 (CDK-1; PDB ID: 5hq0) with a score of 15.08 and human cyclin-dependent kinase 2 (CDK-2; PDB ID: 1g5s) with a score of 16.03 as the top-ranking and, notably, the only protein targets exceeding the threshold, suggesting their potential involvement in the compound's anticancer effects. Cyclin-dependent kinases 1 and 2 (CDK1 and CDK2) are pivotal enzymes in regulating the cell cycle, with CDK1 primarily governing the G2/M transition and CDK2 facilitating the G1/S transition [39]. Due to their central roles in cell proliferation, CDK1 and CDK2 are recognized as significant targets in

anticancer drug development, as their inhibition can effectively halt the growth of cancer cells.

2.2.6.2. Molecular Docking and Dynamics Study.

Molecular docking studies were conducted using a generated three-dimensional model of the target compound to elucidate its binding interactions with CDK1 and CDK2. This computational approach allows for the prediction of the compound's orientation and affinity within the active sites of these two kinases. To identify the most stable binding mode within the enzyme's active site, the top ten docking poses were further evaluated through short (30 ns) molecular dynamics simulations. The pose exhibiting the most favorable docking score (-12.33 kcal/mol) also displayed the highest stability throughout the simulation, evidenced by its lowest average root-mean-square deviation (RMSD) of 1.92 Å. Based on its favorable docking score and superior stability in the initial short simulations, this specific binding pose was chosen for an extended 200-ns molecular dynamics simulation. This longer simulation aimed to provide a more in-depth understanding of the target compound's binding dynamics within the active sites of both CDK-1 and CDK-2.

Focusing on CDK1:

Regarding CDK1, the 200 ns simulation revealed that the target compound's RMSD profile was similar to that of the co-crystallized inhibitor, with average fluctuations of approximately 1.98 Å and 2.32 Å, respectively (Figure 9, Figure 7C). This comparable stability in binding was further supported by their similar calculated absolute binding free energies (ΔGBind), which were -9.12 kcal/mol for the target compound and -8.51 kcal/mol for the co-crystallized inhibitor. A more detailed examination of their binding interactions showed that the predicted binding mode of the target compound within CDK1 differed from that observed for the co-crystallized inhibitor (Figures 10A and 10B). Analysis of the target compound's binding mode within the CDK1 active site indicated that hydrophobic interactions were the primary driving force for its association. Specifically, the compound established four hydrophobic contacts involving the amino acid residues ILE-10, VAL-64, PHE-80 (via π-π stacking), and Leu-153. The target compound interacted with the CDK1 active site mainly through hydrophobic contacts (ILE-10, VAL-64, PHE-80, Leu-153) and two hydrogen bonds (ASP-86, LYS-88). The co-crystallized inhibitor, in comparison, formed three hydrophobic contacts (TYR-15, VAL-18, LEU-135) and only one hydrogen bond (LEU-83). This difference in hydrogen bonding, with the target compound having more, might account for the co-crystallized inhibitor's decreased stability (increased RMSD after 149 ns) during the simulation. Regarding CDK-2, the 200 ns molecular dynamics simulation revealed similar RMSD profiles for the target compound and the co-crystallized inhibitor, both exhibiting average fluctuations of approximately 2.36 Å (Figure 10). This comparable binding stability was further supported by their similar calculated absolute binding free energies (ΔGBind), which were -9.22 kcal/mol for the target compound and -8.49 kcal/mol for the co-crystallized inhibitor. The binding modes of the target compound and the co-crystallized inhibitor in CDK-2 were observed to be different upon further analysis (Figures 10A and 10B). Within the CDK-2 active site, the target compound's binding was predominantly driven by hydrophobic interactions, forming six stable contacts with ILE-10, VAL-18, VAL-64, PHE-80 (via π-π stacking), LEU-134, and ALA-144. The co-crystallized inhibitor also exhibited several hydrophobic interactions involving similar residues. Regarding hydrogen bonding, the target compound established three stable hydrogen bonds with the main chain of ILE-10, as well as with the side chains of ASP-86 and GLN-131. Comparatively, the co-crystallized inhibitor also formed three hydrogen bonds, but with different residues: the main chain of LEU-83, and the side chains of ASN-132 and ASP-145. Based on the findings from the computational modeling and molecular dynamics simulations, it is reasonable to

 DOI:10.21608/MERMJ.2025.380096.1025

conclude that the anticancer effects of the target compound are likely mediated through its interaction with and inhibition of both CDK-1 and CDK-2.

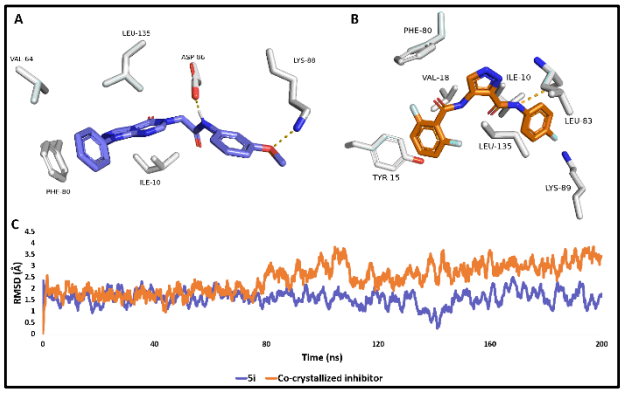

Figure 9. Panels **A** and **B** depict the most frequent binding orientations (poses) of the target compound within the CDK-1 binding site (PDB ID: 5hq0), shown alongside the pose of the co-crystallized inhibitor. Panel C presents the root mean square deviations (RMSDs) of both the target compound and the co-crystallized inhibitor within the CDK-1 binding site throughout a 200-nanosecond molecular dynamics (MD) simulation.

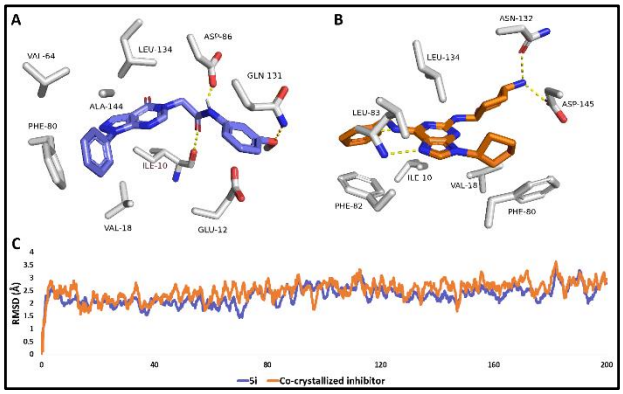

Figure 10. A and **B:** The most populated poses of the target compound inside the binding site of CDK-2 (PDB ID: 1g5s) compared with that of the co-crystallized inhibitor**. C:** RMSDs of the target compound inside the binding site of CDK-2 inclusion, that of the co-crystallized inhibitor by 200 200-ns-long MD simulation.

2.2.7. Predicted Physicochemical Properties and Toxicity Parameters

To be a viable drug, a compound needs acceptable pharmacokinetic properties. Therefore, the physicochemical and pharmacokinetic characteristics of the synthesized derivatives, including the target compound, were predicted using Swiss ADME (**Tables 6-10**, **Figs.13)**. Because the target molecule is unlikely to cross the blood-brain barrier, it is expected to have high gastrointestinal absorption and a minimal risk of central nervous system adverse effects. Furthermore, the target compound's expected influence on important CYP450 enzymes indicates a low probability of drug-drug interactions. The target chemical also has a molecular weight less than 500 g/mol. Notably, the synthesized compound satisfies the Ghose filter criteria, showing no deviations. The synthesized compound demonstrates favorable drug-like properties by satisfying the Veber, Egan, and Muegge filters without any violations. It is predicted Abbott bioavailability score indicates good oral absorption. An examination of its physicochemical properties using a bioavailability radar showed that the compound possesses acceptable size (150-500 g/mol), reasonable polarity (TPSA 20-130 Å²), adequate solubility (Log S (ESOL) -6 to 0), and sufficient flexibility (less than 9 rotatable bonds). However, its lipophilicity (XLOGP3 outside -0.7 to +5.0) and degree of saturation (Fraction Csp3 outside 0.25 to 1.0) are outside the recommended ranges. Moreover, predictions from the BOILED-Egg model suggest significant gastrointestinal absorption and a low probability of crossing the blood-brain barrier, potentially indicating good central nervous system safety.

Compound	MR	Rotatable bonds	HBAs	Aromatic heavy atoms	Fraction csp3	HBDs	Heavy atoms	TPSA
The target compound	104.7	6	5	27	0.04	1	28	91.041

Table 5. Physicochemical attributes of the synthesized compound

Compound	WLOGP	XLOGP3	Ilogp	MLOGP	Silicos-IT LogP	Consensus Log P
The target compound	2.04	2.07	2.80	2.17	1.52	2.12

Table 6. Lipophilicity profile of the synthesized compound

Compound	Ali Solubility mg/mL	ESOL solubility mg/ml	Silicos-IT Solubility mg/ml	Ali Class	ESOL Class	Silicos-IT class
The target compound	9.19	8.79	4.39	Soluble	Soluble	Moderately Soluble

Table 7. Water solubility analysis of the synthesized compound

Compound	CYP2C19 Inhibitor	Log Kp Cm/s	Pgp substrate	CYP1A2 Inhibitor	CYP2C9 Inhibitor	GI absorption	CYP2D6 inhibitor	CYP3A4 inhibitor	BBB permanent
The target compound	YES	-7.12	NO	NO	NO	High	NO	YES	No

Table 8: Evaluation of the compound's pharmacokinetics

Compound	Veber violation	Egan violation	Mugge violation	Lipinski violations	Ghose violations	Bioavalability
The target compound	0	0	0	0	0	0.55

Table 9: Assessment of drug-likeness

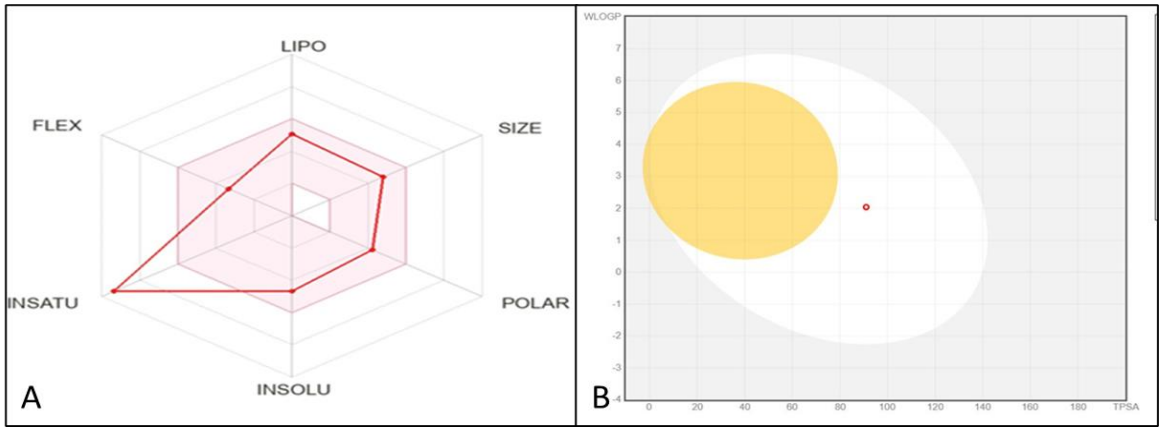

Figure 9. (A) Rader model for target compound, and (B) the BOILED-Egg model of the target compound.

4. Experimental

4.1. Chemistry

The progress of reactions was tracked using TLC, with compounds visualized by UV light at 254 nm. Uncorrected melting points were determined using a Stuart Scientific Co. Melting points were determined using an electrothermal apparatus. Infrared (IR) spectra (KBr discs) were recorded on a Shimadzu 408 Spectrophotometer at Sohag University. NMR Spectra (400 MHz) were obtained on a Bruker AM NMR spectrometer at the same institution, with chemical shifts (ppm) referenced to TMS. Elemental microanalyses for carbon, nitrogen, and hydrogen were performed at Al-Azhar University in Cairo.

4.1.1. Synthesis of

2-(ethoxymethylene) malononitrile (1)

As previously described [25], an equimolar mixture of malononitrile and ethyl orthoformate (2 mmol each), along with acetic anhydride (3 mmol), was heated under reflux at 110 °C for 4 hours.

White powder; yield: 1.74 g (78%); mp 66-67 °C (reported 66-68 °C)

4.1.2. Synthesis of 5-amino-1-phenyl-1*H*-pyrazole-4-*carbonitrile* (2)

Compound 1 (1.22 g, 1 mmol) and the appropriate 4-substituted phenyl hydrazine (1.08 g, 1 mmol) were combined in ethanol (5 mL) in a round-bottomed flask and heated under reflux for 18 hours. The reaction mixture was then cooled, and the solvent volume was reduced by half. Following further cooling, the resulting crystals were collected by filtration, dried, and purified by recrystallization from methanol [26]. White powder; yield: 1.29 g, (70%); mp 142-143 °C (as reported 140-142) [26].

4.1.3. Synthesis of 1-phenyl-1,5-dihydro-*4H*-pyrazolo[3,4-d]pyrimidin-4-one (3)

Compound 2 (0.92 g, 0.5 mmol) was heated under reflux in formic acid for 4 hours. Upon cooling, the resulting solid was collected by filtration, washed thoroughly, and dried. Pure product was obtained after recrystallization from ethanol [26]. White powder, yield: 0.98 g, (92%); mp 270-272 °C (as reported) [26].

4.1.4. Synthesis of 2-chloro-*N*-(3-methoxyphenyl) Acetamide (4)

Brown powder; yield: (0.90 g, 89%); mp: 119-121°C reported mp: 121-122 °C [28].

4.1.5. synthesis of *N*-(3-methoxyphenyl)-2-(4-oxo-1-phenyl-1,4-dihydro-5*H*-pyrazolo[3,4d]pyrimidin-5-yl)Acetamide (The target compound)

In DMF, a stirred mixture of compound 3 (0.53 g, 0.25 mmol) and potassium carbonate (0.690 g, 5 mmol) was treated with 2-chloro-N-(3-methoxyphenyl)acetamide4 (0.60 g, 0.3 mmol). The

resulting solution was heated under reflux for 8 hours. Following this, the reaction mixture was poured onto crushed ice, and the reaction's completion was monitored by TLC using a dichloromethane/ethanol mixture (19:1) as the eluent. The precipitated solid was then collected by filtration, washed with water, dried, and purified by recrystallization from ethanol to yield the desired product [29]. Greyish white powder, yield: 0.57 g (60.8%), m.p.: 228-230˚C; IR (KBr, cm^{-1}): 3328(NH), 1679,1702(C═O) ^{1}H NMR (400 MHz, DMSO-d_6): δ (ppm) 10.48 (s, IH, N-H) 8.52 (s, 1H, pyrimidine-H); 8.41 (s, 1H, pyrazole-H), 8.07(d, *J* =8.0 Hz, 2H, Ar-H), 7.62-7.58(m, 2H, Ar-H), 7.44 (t, *J* =8.0 Hz, 1H, Ar-H), 7.32 (d, *J* =8.0 Hz, 1H, Ar-H), 7.40 (t, *J*=8.0 Hz, 1H, Ar-H), 7.12 (t, *J*=8.0 Hz, 1H, Ar-H) 6.68-6.66(m, 1H, Ar-H), 4.93 (s, 2H, CH_2), 3.73(s, 3H, O-CH_3); ^{13}C NMR (100 MHz, DMSO-d_6):δ (ppm):165.84, 160.28, 156.84, 152.54, 152.04, 140,21, 138.82, 136.61, 130.08, 129.81, 127.78, 122.26, 111.74, 109.61, 107.16, 105.23, 55.44, 48.72. Anal.Calcd. For: $C_{20}H_{17}N_5O_3$ C%, 63.99; H%, 4.56; N%, 18.66; Found: C%, 64.17; H%, 4.75; N%, 18.93.

4.2. Biology

4.2.1 .Screening of anti-cancer activity in the (NCI)

The anticancer potential of the synthesized compound was assessed by the National Cancer Institute (NCI) in Bethesda, USA. This evaluation utilized a panel of 60 distinct cell lines, representing nine prevalent human cancer types available within the NCI's collection, organized into nine sub-panels. Detailed information regarding the screening procedures employed by the National Cancer Institute (NCI) is available on their website (http://www.dtp.nci.nih.gov). Further information can also be found in Appendix A of the Supplementary Materials.

4.2.2. the IC50 evaluation of the target compound in HOP-92, RXF393, and WI 38 cell lines.

Using standard MTT assay protocols, the half-maximal inhibitory concentration (IC50) of the target compound was evaluated in the HOP-92 and RXF393 cancer cell lines and the WI-38 normal cell line. For a more comprehensive explanation of the procedure, please refer to Appendix A in the Supplementary Materials.

4.2.3. Invitro assay of CDK1/2 inhibition.

The activity of cyclin-dependent kinases (CDKs), crucial enzymes in cell cycle control, is dependent on their interaction with regulatory cyclins. The precise regulation of these kinases is vital for accurate cell division. Considering that uncontrolled cell division is a key feature of cancer, modulating CDK activity represents a potential therapeutic intervention. Specifically, CDK1 is essential for the progression of mitosis [33The activity of CDK1/Cyclin B1 was assessed using a CDK1 Assay Kit that utilizes Kinase-Glo® MAX for detection, suitable for screening and profiling. This kit, provided in a 96-well format, contains the necessary purified recombinant CDK1/Cyclin B1 enzyme, CDK substrate peptide, ATP, and kinase assay buffer for 100 assays. The inhibitory potential of compounds against CDK1/2 was evaluated in vitro using a commercially available kit from BPS Bioscience Inc. (San Diego, CA, USA). Additionally, CDK2 plays a crucial role in DNA replication. Similar to the CDK1 kit, the CDK2 Assay Kit measures CDK2/Cyclin A2 activity using Kinase-Glo MAX and is also supplied in a 96-well format with sufficient reagents for 100 assays. Further details regarding these assay kits can be found in Appendix A of the Supplementary Materials

4.2.4. Cell cycle analysis

The impact of the target compound on cell cycle phase distribution was investigated in human renal (RXF-393) and non-small cell lung (HOP-92) cancer cells. DNA content was quantified using the Propidium Iodide Flow Cytometry Kit to assess the compound's influence on cell cycle progression in

these cell lines, following established protocols. More comprehensive information regarding the experimental procedures is available in Appendix A of the Supplementary Materials.

4.2.5. Apoptosis Determination

Following established protocols, the Annexin V-FITC Apoptosis Detection Kit (Bio Vision Research Products, USA) was used to evaluate the target compound's ability to induce apoptosis. Further details regarding the experimental procedure can be found in Appendix A of the Supplementary Materials.

4.2.6. Molecular docking

For molecular docking, the crystal structures of CDK-1 (PDB ID: 5hq0) and CDK-2 (PDB ID: 1g5s) were obtained and used with AutoDock Vina [40, 41]. The binding sites were defined based on co-crystallized ligands, and grid boxes were centered at specific coordinates (CDK-1: x = 3.26, y = 47.98, z = 27.55; CDK-2: x = 61.66, y = 33.51, z = 17.42). Ligand conformations within 2.0 Å RMSD of the binding site were considered. The Charmm force field (version 1.02) was employed to calculate interaction energies (10.0 Å non-bonded cutoff, distance-dependent dielectric). An energy grid (5.0 Å extension from the binding site) was established, and the compound retinol was energy-minimized within it. PyMOL software [42] was used for analysis and visualization of the resulting binding poses.

4.2.1. Molecular Dynamics Simulation

Molecular dynamics (MD) simulations were performed with NAMD 3.0.0 [43] and the Charmm-36 force field. Protein systems were prepared using VMD's QwikMD [44] (adding hydrogens, setting pH 7.4 protonation, removing water), solvated in TIP3P water in an orthorhombic box (20 Å layer), and neutralized with 0.15 M Na+/Cl-. The systems were then energy-minimized and equilibrated for 5 ns. Ligand parameters and topology were generated with VMD's ffTK plugin [45] to set up protein–ligand complexes for simulation.

4.3.2. Binding Free Energy Calculations

The Molecular Mechanics Poisson-Boltzmann Surface Area (MM-PBSA) method, implemented in the MMPBSA.py module of AMBER18 [46], was used to calculate the binding free energy (ΔG Binding) of the complex obtained from docking studies, allowing for a better understanding of the protein-ligand interaction. This calculation involved analyzing 100 snapshots from the MD simulation and was determined using the equation: \Delta G_{Binding} = \Delta G_{Complex} - (\Delta G_{Receptor} + \Delta G_{Inhibitor}). The individual energy terms were estimated considering van der Waals and electrostatic contributions, internal energy, and the polar solvation energy derived from the Poisson-Boltzmann equation.

4.4. Physicochemical and pharmacokinetic prediction

To predict the target compound's physicochemical and pharmacokinetic characteristics, the freely accessible SwissADME web server [47] was used. The BOILED-Egg plot, which visually distinguishes compounds with high predicted gastrointestinal (GI) absorption (white area) from those likely to cross the blood-brain barrier (BBB) (yolk) based on TPSA and WLOGP, was generated. Lipophilicity was determined using the consensus log Po/w from SwissADME, an average of multiple log P predictions. A bioavailability profile, visualizing six crucial physicochemical properties. Against their optimal ranges (central pink hexagon) was also utilized. Finally, the Lipinski filter (molecular weight < 500, MLOGP ≤ 4.15, ≤ 10 N or O atoms, ≤ 5 hydrogen bond donors) was applied to evaluate the compound's drug-likeness.

5. Conclusion

In summary, a novel pyrazolo-pyrimidine derivative was successfully synthesized and demonstrated significant anticancer activity, particularly against

RXF-393 and HOP-92 cell lines, consistent with NCI screening results. MTT assays confirmed its potent cytotoxicity, and mechanistic studies revealed cell cycle arrest at different phases (G1 in RXF-393, G2/M in HOP-92) and the induction of apoptosis and necrosis. Notably, the compound exhibited strong in vitro inhibition of CDK1 and CDK2, surpassing the potency of roscovitine in molecular docking studies. In silico analysis further suggested favorable drug-like and physicochemical properties. These findings highlight the significant potential of this novel pyrazolo-pyrimidine derivative as a promising lead for developing CDK1/2 inhibitors in cancer therapy, warranting further preclinical and clinical investigation.

References

1 Mohamed, M.F., et al., Synthesis, anticancer and anti-inflammatory evaluation of novel quinoxaline-1, 3, 4-oxadiazole derivatives as EGFR and COX-2 inhibitors. Journal of Molecular Structure, 2025: p. 141651.

2. Ibrahim, A.S., et al., Cancer Incidence in Egypt: Results of the National Population-Based Cancer Registry Program. Journal of Cancer Epidemiology, 2014. 2014(1): p. 437971.

3. Alharthy, R.D., Design and Synthesis of Novel Pyrazolo[3,4-d]Pyrimidines: In Vitro Cytotoxic Evaluation and Free Radical Scavenging Activity Studies. Pharmaceutical Chemistry Journal, 2020. 54(3): p. 273-278.

4. Atatreh, N., et al., Anti-inflammatory drug approach: Synthesis and biological evaluation of novel pyrazolo[3,4-d]pyrimidine compounds. Bioorg Chem, 2019. 86: p. 393-400.

5. Sureja, D.K., S.P. Dholakia, and K.R. Vadalia, Synthesis of some novel pyrazolo[3,4-d] pyrimidin-4(5H)-one derivatives as potential antimicrobial agents. J Pharm Bioallied Sci, 2016. 8(4): p. 321-326.

6. Trivedi, A., et al., Synthesis and antimycobacterial evaluation of various 6-substituted pyrazolo[3,4-d]pyrimidine derivatives. J Enzyme Inhib Med Chem, 2010. 25(6): p. 893-9.

7. Smee, D.F., et al., Novel pyrazolo[3,4-d]pyrimidine nucleoside analog with broad-spectrum antiviral activity. Antimicrob Agents Chemother, 1987. 31(10): p. 1535-41.

8.Rosemeyer, H., M. Anders, and F. Seela, Symmetrically and Unsymmetrically Bridged Methylenebis(allopurinols): Synthesis of Dimeric Potential Anti-Gout Drugs. Molecules, 2007. 12(3): p. 563-575.

9.Reddy, B.N., et al., Novel Pyrazolo [3, 4-d] pyrimidine-Containing Amide Derivatives: Synthesis, Molecular Docking, In Vitro and In Vivo Antidiabetic Activity. ChemistrySelect, 2019. 4(34): p. 10072-10078.

10. Salem, I.M., et al., A review on Synthesis and Biological Evaluations of Pyrazolo[3,4-d]pyrimidine Schaffold %J Records of Pharmaceutical and Biomedical Sciences. Records of Pharmaceutical and Biomedical Sciences, 2022. 6(1): p. 28-50.

11. Le Brazidec, J.-Y., et al., Synthesis, SAR and biological evaluation of 1,6-disubstituted-1H-pyrazolo[3,4-d]pyrimidines as dual inhibitors of Aurora kinases and CDK1. Bioorganic & Medicinal Chemistry Letters, 2012. 22(5): p. 2070-2074.

12.Cherukupalli, S., et al., Synthesis of 4,6-disubstituted pyrazolo[3,4-d]pyrimidine analogues: Cyclin-dependent kinase 2 (CDK2) inhibition, molecular docking and anticancer evaluation. Journal of Molecular Structure, 2019. 1176: p. 538-551.

13. Rayego-Mateos, S., et al., Role of epidermal growth factor receptor (EGFR) and its ligands in kidney inflammation and damage. Mediators of inflammation, 2018. 2018(1): p. 8739473.

14. Abdelgawad, M.A., et al., Targeting tumor cells with pyrazolo [3, 4-d] pyrimidine scaffold: A literature review on synthetic approaches, structure activity relationship, structural and target-based mechanisms. Arabian Journal of Chemistry, 2022. 15(5): p. 103781.

15.Yin, Y., et al., Structure-based design and synthesis of 1H-pyrazolo [3, 4-d] pyrimidin-4-amino derivatives as Janus kinase 3 inhibitors. Bioorganic Medicinal Chemistry, 2018. 26(17): p. 4774-4786.

16. Massacci, G., L. Perfetto, and F. Sacco, The Cyclin-dependent kinase 1: more than a cell cycle regulator. British Journal of Cancer, 2023. 129(11): p. 1707-1716.

17. Talatam, A., et al., Targeting overexpressed cyclin-dependent kinase 1 (CDK1) in human cancers: Kamalachalcone A emerged as a potential inhibitor of CDK1 kinase through an in silico docking study. Oncogen, 2023. 6(1): p. 25.

18. Husseiny, E.M., Synthesis, cytotoxicity of some pyrazoles and pyrazolo[1,5-a]pyrimidines bearing benzothiazole moiety and investigation of their mechanism of action. Bioorganic Chemistry, 2020. 102: p. 104053.

19.Nassar, I.F., et al., Discovery of pyrazolo [3, 4-d] pyrimidine and pyrazolo [4, 3-e][1, 2, 4] triazolo [1, 5-c] pyrimidine derivatives as novel CDK2 inhibitors: synthesis, biological and molecular modeling investigations. RSC Advances, 2022. 12(23): p. 14865-14882.

20.Zaki, W.A., et al., Design, Synthesis, In Vitro, and Silico Studies of New N5-Substituted-pyrazolo[3,4-d]pyrimidinone Derivatives as Anticancer CDK2 Inhibitors. pharmceuticals. 2023. 16(11): p. 1593.

21.Villerbu, N., et al., Cellular effects of purvalanol A: A specific inhibitor of cyclin-dependent kinase activities. International journal of cancer, 2002. 97(6): p. 761-769.

22.Finn, R.S., et al., Palbociclib and letrozole in advanced breast cancer. New England journal of medicine, 2016. 375(20): p. 1925-1936.

23.Cicenas, J., et al., Roscovitine in cancer and other diseases. Annals of translational medicine, 2015. 3(10).

24.Hamed, O.A., et al., Molecular docking approach for the design and synthesis of new pyrazolopyrimidine analogs of roscovitine as potential CDK2 inhibitors endowed with pronounced anticancer activity. Bioorganic Chemistry, 2024. 147: p. 107413.

25.Ding, R., et al., Preparation and bioevaluation of 99m Tc nitrido radiopharmaceuticals with pyrazolo [1, 5-a] pyrimidine as tumor imaging agents. Medicinal Chemistry Research, 2012. 21: p. 523-530.

26.Somakala, K., S. Tariq, and M.J.B.c. Amir, Synthesis, evaluation, and docking of novel pyrazolo pyrimidines as potent p38α MAP kinase inhibitors with improved anti-inflammatory, ulcerogenic, and TNF-α inhibitory properties. Bioorganic chemistry, 2019. 87: p. 550-559.

27.Kumar, R., et al., Synthesis, cytotoxic study and docking-based multidrug resistance modulator potential analysis of 2-(9-oxoacridin-10 (9H)-yl)-N-phenyl acetamides. European Journal of Medicinal Chemistry. 2014. 80: p. 83-91.

28.Modh, R.P., et al., Design, Synthesis, Biological Evaluation, and Molecular Modeling of Coumarin–P iperazine Derivatives as Acetylcholinesterase Inhibitors. Archiv der Pharmazie, 2013. 346(11): p. 793-804.

29.Hafez, H.N. and A.-R.B.J.M. El-Gazzar, Synthesis and biological evaluation of N-pyrazolyl derivatives and pyrazolopyrimidine bearing a biologically active sulfonamide moiety as potential antimicrobial agents. Molecules, 2016. 21(9): p. 1156.

30.Kuthati, B., et al., Synthesis of novel spiro [pyrazolo [4, 3-d] pyrimidinones and spiro [benzo [4, 5] thieno [2, 3-d] pyrimidine-2, 3′-indoline]-2′, 4 (3H)-diones and their evaluation for anticancer activity. Bioorganic Medicinal Chemistry Letters, 2017. 27(6): p. 1446-1450.

31.Mohamed, M.F. and G.E.-D.A.J.R. Abuo-Rahma, Molecular targets and anticancer activity of quinoline–chalcone hybrids: Literature review. RSC Advances, 2020. 10(52): p. 31139-31155.

32.Reda, N., et al., Novel Pyrimidine-5-Carbonitriles as potential apoptotic and antiproliferative agents by dual inhibition of EGFRWT/T790M and PI3k enzymes; Design, Synthesis, biological Evaluation, and docking studies. Bioorganic Chemistry, 2024. 145: p. 107185.

33.Abdelgawad, M.A., et al., Design, synthesis, and antitumor activity of novel pyrazolo [3, 4-d] pyrimidine derivatives as EGFR-TK inhibitors. Bioorganic Chemistry, 2016. 66: p. 88-96.

34.Esquer, H., Q. Zhou, and D.V.J.C. LaBarbera, Targeted Inhibition of CHD1L by OTI-611 Reprograms Chemotherapy and Targeted Therapy-Induced Cell Cycle Arrest and Suppresses Proliferation to Produce Synergistic Antitumor Effects in Breast and Colorectal Cancer. Cells, 2025. 14(5): p. 318.

35.Elmore, S.J.T.P., Apoptosis: a review of programmed cell death. Toxicologic pathology, 2007. 35(4): p. 495-516.

36.Wang, X., et al., PharmMapper 2017 update: a web server for potential drug target identification with a comprehensive target pharmacophore database. Nucleic Acids Res, 2017. 45(W1): p. W356-w360.

37.Brown, N.R., et al., CDK1 structures reveal conserved and unique features of the essential cell cycle CDK. Nat Commun, 2015. 6: p. 6769.

38.Dreyer, M.K., et al., Crystal structure of human cyclin-dependent kinase 2 in complex with the adenine-derived inhibitor H717. Journal of Medicinal Chemistry, 2001. 44(4): p. 524-530.

39.Sakurikar, N. and A.J.C.C. Eastman, Critical reanalysis of the methods that discriminate the activity of CDK2 from CDK1. Cell Cycle, 2016. 15(9): p. 1184-1188.

40.Huey, R., G.M. Morris, and S.J.T.S.R.I.M.G.L. Forli, Using AutoDock 4 and AutoDock vina with AutoDockTools: a tutorial. The Scripps Research Institute Molecular Graphics Laboratory 2012. 10550(92037): p. 1000.

41.Rimon, G., et al., Coxibs interfere with the action of aspirin by binding tightly to one monomer of cyclooxygenase-1. Proceedings of the National Academy of Sciences of the United States of America, 2010. 107(1): p. 28-33.

42.Yuan, S., H.S. Chan, and Z.J.W.I.R.C.M.S. Hu, Using PyMOL as a platform for computational drug design. Computational Molecular Science, 2017. 7(2): p. e1298.

43.Phillips, J.C., et al., Scalable molecular dynamics with NAMD. Journal of Computational Chemistry 2005. 26(16): p. 1781-1802.

44.Saidi, A.E., et al., In silico and in vitro studies: investigating the chemical composition, DFT, molecular docking, and dynamic simulation of Satureja candidissima (Munby) Briq essential oil as a potential antibacterial agent. Journal of Biomolecular Structure Dynamics.2024: p. 1-20.

45.Humphrey, W., A. Dalke, and K.J.J.o.m.g Schulten, VMD: visual molecular dynamics. Journal of Molecular Graphics 1996. 14(1): p. 33-38.

46.Miller III, B.R., et al., MMPBSA. Py: an efficient program for end-state free energy calculations. Journal of chemical theory and computation 2012. 8(9): p. 3314-3321

47.Al-Hakkani, M.F., et al., Synthesis, Physicochemical Characterization using a Facile Validated HPLC Quantitation Analysis Method of 4-Chloro-phenylcarbamoyl-methyl Ciprofloxacin and Its Biological Investigations. International Journal of Molecular Sciences 2023. 24(19): p. 14818.

Corresponding author: Mostafa Roshdi Kobesy Helal

Department of pharmaceutical chemistry, faculty of pharmacy

E-mail: Mostafa.roshdi1997@gmail.com

Phone: 01271717196